J. Fluid Mech. (2017), *vol.* 830, R1, doi:10.1017/jfm.2017.627

JFM RAPIDS
journals.cambridge.org/rapids



Sharp acceleration of a macroscopic contact line induced by a particle

Lizhong Mu[1,2], Daichi Kondo[3], Motochika Inoue[3], Toshihiro Kaneko[4], Harunori N. Yoshikawa[5,†], Farzam Zoueshtiagh[6] and Ichiro Ueno[4,†]

[1]Research Institute for Science and Technology, Tokyo University of Science, Chiba 278-8510, Japan

[2]Key laboratory of Ocean Energy Utilization and Energy Conservation of Ministry of Education, School of Energy and Power Engineering, Dalian University of Technology, Dalian, 116024, China

[3]Division of Mechanical Engineering, Graduate School of Science and Technology, Tokyo University of Science, Chiba 278-8510, Japan

[4]Department of Mechanical Engineering, Faculty of Science and Technology, Tokyo University of Science, Chiba 278-8510, Japan

[5]Université Côte d'Azur, CNRS, UMR 7351, Laboratoire J.-A. Dieudonné, 06108 Nice Cedex 02, France

[6]Univ. Lille, CNRS, ECLille, ISEN, Univ. Valenciennes, UMR 8520 - IEMN, F-59000 Lille, France

(Received 17 April 2017; revised 31 July 2017; accepted 1 September 2017; first published online 29 September 2017)

Wetting of a planar solid substrate is investigated in the presence of a macroscopic particle in the complete wetting regime. A drop of silicone oil spreads on the substrate and its macroscopic edge is incident on the particle at the late stage of spreading. The drop–particle interaction is observed in detail by shadowgraph and interferometry. Although the spreading drop edge is pinned by the particle for a short time, a sharp acceleration occurs when the liquid starts wetting the extra surface area offered by the particle and forming a meniscus. This process yields a net gain in spreading speed. A theoretical model based on the classical wetting dynamics dictated by Cox's law is developed. It predicts that the capillary energy of the meniscus gives rise to a rapid motion of the liquid edge, showing good agreement with the dynamics observed in the experiments.

Key words: capillary flows, contact lines, drops

1. Introduction

Wetting is a ubiquitous phenomenon in nature (de Gennes, Brochard-Wyart & Quéré 2002), which has primary interest in a wide variety of industrial, medical and technological applications. Many biological systems benefit from their multifunctional,

† Email addresses for correspondence: harunori@unice.fr, ich@rs.tus.ac.jp

© Cambridge University Press 2017

https://doi.org/10.1017/jfm.2017.627 Published online by Cambridge University Press

protective surfaces due to particular wetting properties such as the self-cleaning ability of lotus leaves (Bhushan, Jung & Koch 2009) or the beneficial wetting properties of some insects (Wagner, Neinhuis & Barthlott 1996). Within numerous industrial applications, one can cite the foremost importance of surface wettability in, for example, lens coating, water-resistant fabric, Lab-on-a-chip devices, inkjet printing or pesticide deposition on plant leaves (de Gennes *et al.* 2002; Bonn *et al.* 2009; Snoeijer & Eggers 2010; Popescu *et al.* 2012).

The wettability of a surface can be quantified through the spreading parameter S_0, which is the difference of surface energies per unit area between dry and wetted surfaces: $S_0 = \gamma_{SO} - \gamma_{SL} - \gamma$, where γ_{SO}, γ_{SL} and γ are the interfacial tensions of solid–gas, solid–liquid and liquid–gas interfaces, respectively (e.g., de Gennes *et al.* 2002). The wetting mechanism of a solid surface is well understood on both the macroscopic and mesoscopic scales, at least, for surfaces of simple geometries and simple chemical properties. A drop of non-volatile liquid placed on a planar, homogeneous, inert substrate is the simplest configuration of wetting. When $S_0 < 0$, the drop relaxes to a thermodynamic equilibrium state to form an equilibrium contact angle θ_E between the liquid–gas and solid–liquid interfaces. The angle θ_E is dictated by Young's equation: $\gamma \cos\theta_E = \gamma_{SO} - \gamma_{SL}$. When $S_0 > 0$, the equilibrium contact angle is $\theta_E = 0$ so that, if the volume of liquid were not limited, the liquid would cover the whole available surface to form a macroscopic film on the substrate. The advancing front of a spreading drop consists of the macroscopic edge of the bulk drop and the microscopic or mesoscopic precursor film emanating from the edge. These two parts are linked by a drop foot of mesoscopic dimension, where a macroscopic contact line (MCL) is observed. The precursor film advances much faster than the MCL and guides the latter, until the liquid forms either an unbounded molecular thin film, or a 'pancake', depending on the nature of short-ranged molecular interactions. At the late stage of spreading, where all transient behaviour related with initial conditions has vanished, the apparent contact angle θ between the substrate and the liquid–gas interface at the MCL is tiny and the drop edge advances in the shape of a wedge. The dynamics of the liquid wedge is characterised by the capillary number $Ca = \mu U/\gamma$, where μ and U are the dynamic viscosity of the liquid and the velocity of the MCL, respectively. The capillary number is correlated with the contact angle by Cox's law as $Ca \propto \theta^3$ (Cox 1986). Coupling it with the volume conservation of the drop, one can derive power laws for the spreading radius R and the contact angle θ (Lopez, Miller & Ruckenstein 1976; Popescu *et al.* 2012):

$$R \sim V^{3\alpha}\left(\frac{\mathcal{F}}{\mu}t'\right)^{\alpha}, \quad \theta \sim V^{\alpha}\left(\frac{\mathcal{F}}{\gamma}\right)^{1/3}\left(\frac{\mathcal{F}}{\mu}t'\right)^{-(1-\alpha)/3}, \tag{1.1a,b}$$

where t' is the time elapsed since the drop deposition and V is the volume of the drop. The symbol $\mathcal{F}$ stands for either γ or ρg. If the radius R is smaller than the capillary length $\ell_c = (\gamma/\rho g)^{1/2}$, the bulk drop takes a spherical-cap shape and the spreading is driven by capillarity. Then, $\mathcal{F} = \gamma$ and $\alpha = 1/10$, and equation (1.1) recovers Tanner's law (Voinov 1976; Tanner 1979; Marmur 1983). If $R \gtrsim \ell_c$, the drop is in a squeezed shape. Then gravity induces the spreading and $\mathcal{F} = \rho g$. The exponent α becomes $\alpha = 1/8$ (Lopez *et al.* 1976).

Hervet & de Gennes (1984) showed that the energy difference S_0 is dissipated completely inside the drop foot at the late stage of spreading. The dynamics of complete wetting can thus be described as a macroscopic liquid flow in which are balanced the driving free energy associated with the drop's non-equilibrium shape

https://doi.org/10.1017/jfm.2017.627 Published online by Cambridge University Press

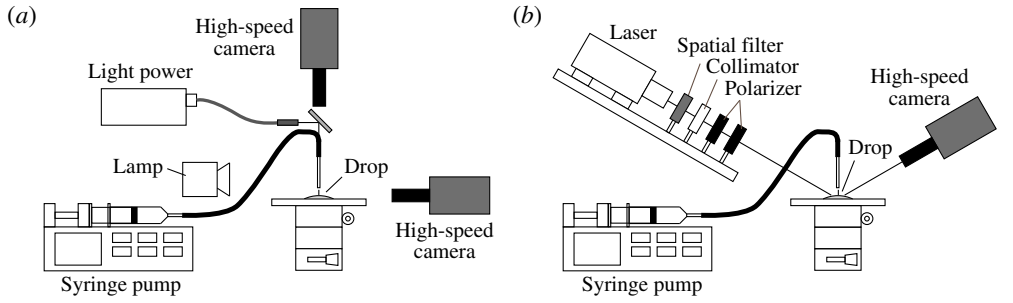


FIGURE 1. Experimental rigs. Different configurations are employed: (*a*) for observation in side and top views and (*b*) for interferometry. In the latter configuration, the optical axis of the camera is tilted from the horizontal by 16°.

and the energy dissipation inside the macroscopic wedge (Hervet & de Gennes 1984; de Gennes 1985). The power laws (1.1), which are independent of S_0, confirm that the spreading is in this quasi-stationary hydrodynamics regime.

Here, we report an experimental investigation of a droplet spreading on a completely wettable surface in the presence of a single spherical particle of a few tens of micrometres in diameter. This configuration can be considered as a disturbance or roughness during the progression of spreading. The investigation is motivated by topological control of surface wettability, which is of primary importance to a wide range of industrial applications: e.g., surface coating, spin-coating in microtechnology, or detergent spraying in surface cleaning procedures. Indeed, Cazabat & Cohen Stuart (1986) demonstrated the importance of substrate roughness in the wetting dynamics. Numerous works have since reported on the equilibrium state and/or dynamics of a drop on different patterned surfaces, such as those with cylindrical micro-pillars (Li, Ma & Lan 2010; Papadopoulos *et al.* 2012), with square micro-pillars (Yuan & Zhao 2013; Wang *et al.* 2015), with hollow square micro-pillars (Dash, Alt & Garimella 2012), or with micro-cones (Liu *et al.* 2014). Unlike these studies investigating collective effects of pillars on the MCL behaviour, the present work is focused on the effect of a single particle deposited on a smooth non-patterned surface. The study is aimed to better understand the physics behind the wetting dynamics involved. The macroscopic drop edge advances on a substrate surface with a tiny contact angle, and in the shape of a wedge, to be incident on a spherical particle. The dynamics of the wedge is investigated experimentally by shadowgraph and interferometry. We describe the experimental set-up in § 2 and present the results in § 3. Section 4 is devoted to a theoretical model. Theoretical predictions are compared to experiments and discussed in § 5. The conclusion and perspectives are given in § 6.

2. Experimental set-up

A drop of silicone oil (polydimethylsiloxane, KF-96L-2cs from Shin-Etsu Chemical Co., Ltd.) of volume $V = 2$ mm^3 is deposited on the horizontal surface of a polished silicon wafer substrate by a syringe pump through a hypodermic needle (figure 1). The oil has a density of $\rho = 873$ kg m^{-3}, a kinematic viscosity of $\nu = 2.00$ mm^2 s^{-1}, and a surface tension of $\gamma = 18.3$ mN m^{-1} at 25 °C. The corresponding capillary length ℓ_c is 1.46 mm. Prior to each experiment, the silicon wafer is cleaned by

https://doi.org/10.1017/jfm.2017.627 Published online by Cambridge University Press

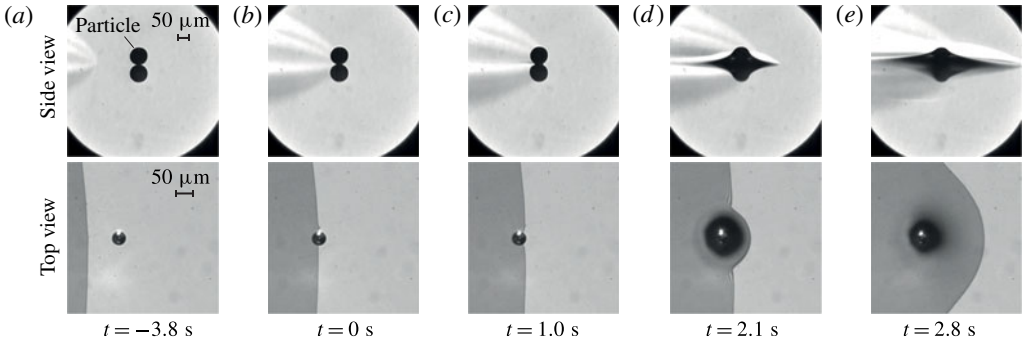


FIGURE 2. Behaviour of an advancing liquid wedge being incident on a spherical particle of diameter 50 μm. The lower half of each side view image is the reflection of the upper part at the substrate surface.

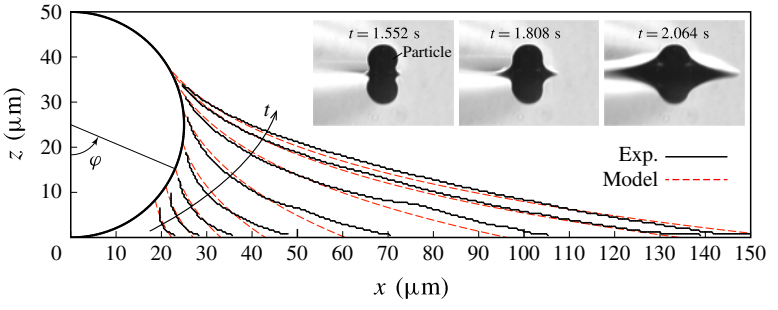


FIGURE 3. Profiles of the meniscus at a particle foot extracted from side view images. The time interval between two profiles is 0.128 s. The first and last profiles are taken at $t = 1.424$ s and $t = 2.320$ s, respectively. Some side view images are shown as insets. The lower half of each inset image is the reflection of the upper part at the substrate surface. Broken-line curves show the profiles predicted by the theoretical model (§ 4) for angular positions φ of MCL-p similar to the experimental ones.

acetone and then by a plasma cleaner (PDC 32G, Harrick Plasma) for a duration of 10 min. A particle is next placed on the substrate at a given distance L (3–4 mm) from the needle position. The particle is a gold-coated acrylic sphere with a diameter in the range from 10 to 50 μm.

Two distinct measuring configurations are employed: one for optical observations from top and side views (figure 1*a*) and another for laser interferometry (figure 1*b*). In the top and side views, the local deformation of the liquid wedge around the particle is monitored (figure 2) by high-speed cameras (Photron, Fastcam-Mini) at a typical frame rate of 250 f.p.s. with a 500× objective lens. A lighting system consisting of a 350 W metal-halide lamp (Photron, HVC-SL) is used. From the recorded side view images, the profile of the air–liquid interface and the angular position φ of the MCL on the particle (hereafter referred to as MCL-p) are determined (figure 3). Laser interferometry is performed to detect the contact angle θ and to follow the motion of the macroscopic contact line at the substrate (hereafter referred to as MCL-s), as shown in figure 4. Laser light of 532 nm wavelength is incident on the advancing liquid wedge through an associated optical system. The resulting fringe pattern is

https://doi.org/10.1017/jfm.2017.627 Published online by Cambridge University Press

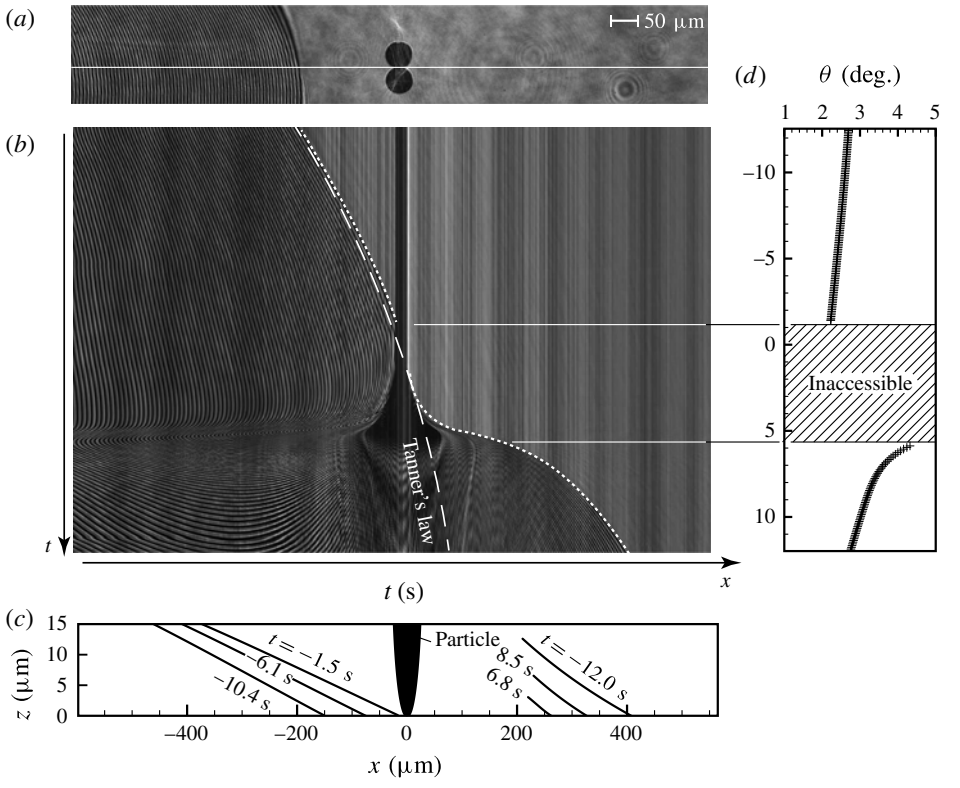


FIGURE 4. An advancing liquid wedge being incident on a spherical particle of diameter 50 μm: (*a*) a typical view of interferometry measurement; (*b*) a space–time diagram; (*c*) profiles of the liquid wedge at different time instants, reconstructed from fringe patterns; (*d*) contact angles measured from the reconstructed profiles at different time instants. The diagram (*b*) is made from thin bands taken from images at different time instants along the white line shown in (*a*). In (*b*), the white dotted curve shows the motion of the macroscopic contact line on the substrate. The white broken line indicates Tanner's law (equation (1.1) with $\alpha = 1/10$).

recorded by the same high-speed camera, but at a tilted optical axis with a lower frame rate of 50 f.p.s. A typical value of the liquid thickness difference between two neighbouring fringes is 0.3 μm. The wedge profile (figure 4*c*) is reconstructed from the pattern to determine θ (figure 4*d*). The contact angle measurement is not possible during a short interval at the incidence of the liquid wedge on the particle due to the obstruction of the laser light by the particle foot. The interferometry views are also used to construct a space-time diagram (figure 4*b*) for tracking the MCL-s position $X(t)$ along the x axis passing through both the drop centre and the particle foot. The velocity of the MCL-s is computed from the temporal evolution of X.

3. Results

A drop injected on the substrate surface spreads out freely on the surface until its advancing MCL reaches the position of a particle, $x = 0$, at a time instant, $t = 0$. For a distance $L = 4$ mm between the deposition point and the particle centre, a

https://doi.org/10.1017/jfm.2017.627 Published online by Cambridge University Press

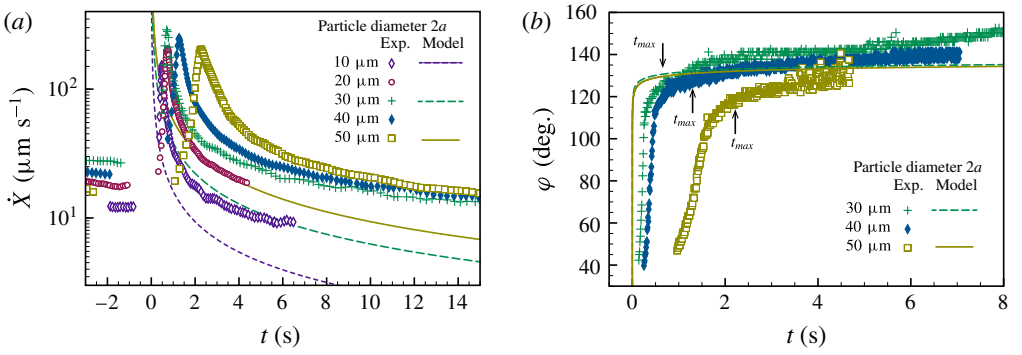


FIGURE 5. Motion of the macroscopic contact lines (MCL): (*a*) the velocity of the MCL on a silicon wafer substrate and (*b*) the angular position of the MCL on a spherical particle. The origin of the time is taken at the formation of the meniscus at the particle foot. Different markers correspond to different particle sizes. Theoretical predictions of the model (§ 4) are shown by different curves. Arrows in (*b*) indicate the experimentally determined times t_{max} of maximum velocity.

time of 30 s is necessary for the drop to spread and reach the particle position. At this moment, the spreading is in the quasi-steady hydrodynamic regime. Indeed, the spreading radius R follows a power law of type (1.1) with an exponent α between 1/10 and 1/8 (figure 4*b*).

After contact with the particle, the MCL-s is deflected locally and pinned by the particle (figure 2*c*) as described by de Gennes (1985) for a contact line at a surface defect. The liquid wedge goes around the particle foot. A meniscus is then formed on the particle, which induces a local axisymmetric deformation of the liquid–air interface around the particle (figure 2*d*). The MCL-s in a semi-circular shape advances on the substrate, while a circular MCL-p ascends along the particle surface (figure 2*d*,*e*). This yields an acceleration of the MCL-s which advances much faster than before the contact (figure 5*a*). Indeed, its velocity reaches approximately 200 μm s^{-1}, which is ten times larger than the incident velocity of approximately 20 μm s^{-1}. This velocity increase is quite sharp, occurring within a short time of the order of 1 s. The time instant $t = t_{max}$ of the maximum MCL-s velocity coincides with the time instant when the MCL-s is approximately one particle diameter ahead the particle centre and when the MCL-p is at an angular position of $\varphi \approx 120°$. The sharp acceleration is then followed by a deceleration. During the deceleration, the MCL-p advances only slightly and converges to its saturation value of $\varphi_\infty \approx 130°$, while the MCL-s advances significantly, following a power law given by

$$X \propto t^{\beta} \quad \text{with } \beta \approx \tfrac{1}{4}. \tag{3.1}$$

This power law is also supported by experiments performed with varying particle position L, which are presented later (figure 7*a*). Through this deceleration, the MCL retrieves Tanner's law (1.1) after it advances approximately ten times the particle diameter far away from the particle.

The liquid–air interface around the particle changes its shape significantly throughout the drop–particle interaction (figure 3). The principal curvature in the x–z plane decreases monotonically with time. The contact angle θ on the substrate also varies significantly (figure 4*d*). The angle θ is approximately 2° before the

https://doi.org/10.1017/jfm.2017.627 Published online by Cambridge University Press

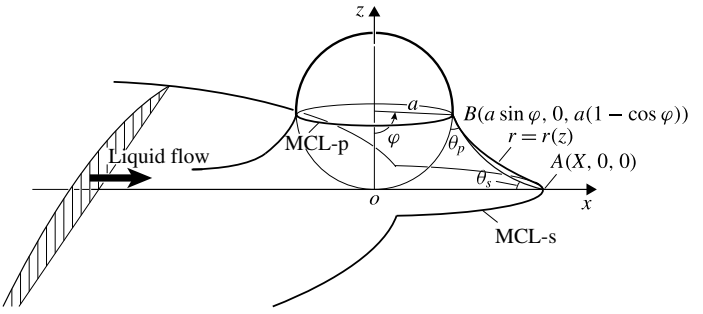


FIGURE 6. Illustration of the geometry of liquid–air interface around a spherical particle.

incidence, while it doubles after the MCL acceleration. It then decays throughout the deceleration phase towards the value it had before the MCL acceleration.

4. A theoretical model

Biance, Clanet & Quéré (2004) and Bird, Mandre & Stone (2008) investigated the early stage of drop spreading on a plane substrate. A meniscus with a strong curvature is formed on the substrate at the cost of the substrate surface energy. The meniscus then releases capillary energy through a relaxation process, which is converted into kinetic energy of the liquid. In the present experiment, the drastic increase of wettable surface area due to the particle results in the formation of a meniscus. It releases energy to accelerate the MCL. Unlike Biance *et al.* (2004) and Bird *et al.* (2008), however, the liquid inertia is negligible compared to the viscosity, as the Reynolds number is small ($Re \sim 10^{-5}$). Hence, we assume instantaneous relaxation of the meniscus. Besides this assumption, we also suppose that the intermolecular forces near the liquid periphery do not alter the meniscus dynamics. In the present experiments, the capillary number Ca also remains small ($Ca \sim 10^{-6}$). The interface shape would thus be determined primarily by capillarity and dictated by the zero local mean-curvature condition: $\mathcal{C} = -r_{zz}(1 + r_z^2)^{-3/2} + r^{-1}(1 + r_z^2)^{-1/2} = 0$, where r is the radial coordinate of the meniscus surface (figure 6) and r_z and r_{zz} stand for the first and second derivatives of r with respect to z. For simplicity, and according to the experimental observation (figure 3), we have assumed an axisymmetric shape of the interface: $r = r(z)$ for its part near the x–z plane. The interface should obey the boundary conditions at the MCLs:

$$z = a(1 - \cos\varphi), \quad r_z = \cot(\theta_p + \varphi) \quad \text{at MCL-p, i.e., at } r = a\sin\varphi; \tag{4.1a,b}$$

$$r = X, \quad r_z = -\cot\theta_s \quad \text{at MCL-s, i.e., at } z = 0. \tag{4.1c,d}$$

The surface shape determined by $\mathcal{C} = 0$ should be coupled with a local dynamical law relating the velocity U and the contact angle θ. The U–θ relation of an advancing contact line has been extensively studied for the case of small capillary number: $Ca \lesssim 0.1$ (Bonn *et al.* 2009). Asymptotic expansions around $Ca = 0$ are applied to the hydrodynamics equations and show that the slope angle θ' of the liquid surface is given by

$$kCa = \int_0^{\theta'} \frac{\chi - \cos\chi\,\sin\chi}{2\sin\chi}\,\mathrm{d}\chi =: g(\theta'). \tag{4.2}$$

https://doi.org/10.1017/jfm.2017.627 Published online by Cambridge University Press

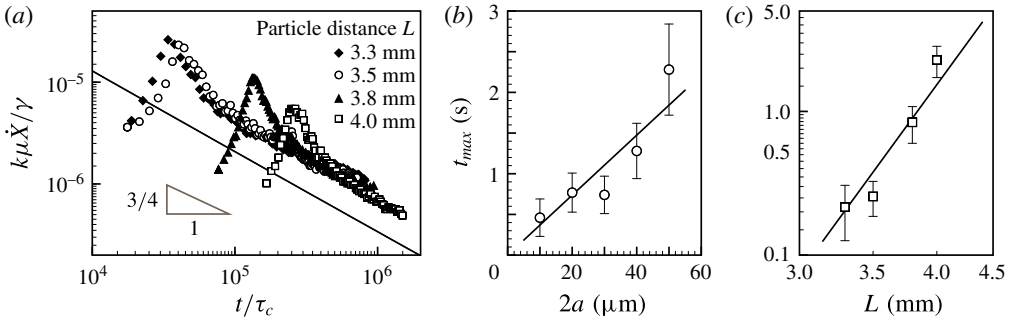


FIGURE 7. The time delay t_{max} for the velocity to attain its maximum value. (*a*) Velocity of the macroscopic contact line on a substrate after the formation of the meniscus around a spherical particle of a diameter 50 μm at different distances L from the drop centre. The time and velocity are scaled by the capillary time $\tau_c = k\mu a/\gamma = 6.4$ μs and a velocity scale $\gamma/k\mu = 3.9$ m s^{-1}. (*b*) Time delay for different particle diameters. The straight line shows a linear fit $t_{max} = 0.0737\,a$. (*c*) Time delay for particles at different distances. A power fit $t_{max} = 7.32 \times 10^{-7} L^{10.5}$ is also shown by a straight line.

The coefficient k is a logarithmic function of the distance ξ measured from the mesoscopic drop foot: $k = \log(\xi/\ell_{min})$. The cutoff length ℓ_{min} characterises the length scale at which the hydrodynamic description ceases to be valid. Since this function varies slowly, k is often considered as constant to give a relationship between the apparent contact angle θ and the velocity U:

$$U = \frac{\gamma}{k\mu}\, g(\theta). \tag{4.3}$$

For a small contact angle, equation (4.3) retrieves Cox's law: $Ca = \theta^3/9k$. The constant k takes a value of the order of 10 (de Gennes *et al.* 2002; Snoeijer & Andreotti 2013). Throughout the present investigation, k is fixed as $k = 8/3$, which corresponds to the value for the dynamical law (4.3) to yield a typically observed MCL-s velocity (20 μm s^{-1}) at a typical contact angle (2°) at the incidence on a particle.

The surface equation $\mathcal{C} = 0$ under the boundary conditions (4.1) and coupled with equation (4.3) forms a complete set of equations to determine the motion of MCLs. Indeed, by solving equation $\mathcal{C} = 0$ under the boundary conditions, one obtains functional relationships between (X, φ) and (θ_s, θ_p) as $\theta_s = \theta_s(X, \varphi)$ and $\theta_p = \theta_p(X, \varphi)$ (appendix A). These relationships coupled with (4.3) applied to MCL-s and MCL-p:

$$\dot{X} = g(\theta_s), \quad \dot{\varphi} = g(\theta_p), \tag{4.4a,b}$$

form a complete set of equations to determine the motion of both MCL-s and MCL-p, where a dot means a time derivative. Equations (4.4*a*,*b*) have been non-dimensionalised with the capillary time scale $\tau_c = k\mu a/\gamma$ and the particle radius a. In the numerical integration of the present model, the initial MCL positions (X_0, φ_0) were taken as $X_0 = 0.1$ and $\varphi_0 = 5.73°$, for which the contact angles θ_s, θ_p are identical to each other. Other values of (X_0, φ_0) have been tested to find that only a narrow range of φ_0 could yield a solution for a given value of X_0 and that the solution is insensitive to the initial condition.

https://doi.org/10.1017/jfm.2017.627 Published online by Cambridge University Press

5. Discussion

Numerical solutions of the theoretical model show behaviour of the meniscus and MCLs similar to the experiment. The meniscus profiles are in good agreement with the experiments (figure 3). The velocity $\dot{X}$ of MCL-s decreases from a maximum value reached immediately after the formation of the meniscus, i.e., at $t=0$ (figure 5*a*). The rate of decrease is larger for smaller particles. The motion of MCL-p occurs on a time scale shorter than that of the MCL-s. Indeed, the angular position φ increases rapidly to saturate at φ_∞ ($\approx 144°$) a few seconds (~ 2 s) after the formation of the meniscus, while the MCL-s velocity $\dot{X}$ continues to decrease even after $t = 10$ s. Taking into account this time-scale separation, one can derive an asymptotic power law for the late relaxation process of MCL-s. When φ is saturated, the functional relationship $\theta_s = \theta_s(X, \varphi)$ is approximated by $\theta_s \approx \sin^2 \varphi_\infty / X$ (appendix A). Substituting this result into equation (4.4*a*,*b*), one can deduce $\dot{X} = \sin^6 \varphi_\infty / 3X^3$ and obtain

$$\frac{X}{a} = \sqrt[4]{\frac{4}{9}\sin^6\varphi_\infty \left(\frac{t}{\tau_c}\right) + \text{cst.}} \approx \sqrt{\frac{2}{3}}\ \sin^{3/2}\varphi_\infty \left(\frac{t}{\tau_c}\right)^{1/4}, \tag{5.1}$$

in a dimensional form. This asymptotic behaviour agrees with the experimental observation $X \propto t^{1/4}$ (3.1).

The agreement between the model and the experiment remains qualitative. Even though the power law (5.1) corresponds to the experimental data (3.1), it underestimates the velocity $\dot{X}$, as seen in figure 5(*a*). This difference may arise from the dynamical law (4.3), which is derived under the assumption of a two-dimensional liquid–air interface. The interface around the particle has, however, a large curvature, in particular at the beginning of particle wetting.

Another difference between the model and experiments is the temporal reactivity of the meniscus. The model predicts the maximum velocity of MCL-s immediately after the formation of the meniscus, while we observe a time delay t_{max} for $\dot{X}$ to reach the maximum. This delay might arise from ignoring the relaxation process of a meniscus in the model. However, a scaling analysis following Biance *et al.* (2004) indicates that the relaxation of the Laplace pressure would occur within a time of the order of $\mu a/\gamma \sim 10^{-6}$ s (appendix B), which is much shorter than the observed time delay. There would be another mechanism that significantly slows down the development of the meniscus. A possible one is slow liquid supply from the bulk drop to the meniscus. The volume of liquid necessary for the meniscus to take a shape corresponding to the maximum velocity will be proportional to the cube of the particle size a. On the other hand, it could also be estimated as the volume transported in the free spreading of a drop: $2a(Ut_{max})^2 \tan\theta \approx 2a(Ut_{max})^2\theta$, where U and θ are the velocity and the contact angle of the drop edge at the particle position and both are dictated by (1.1). Equating these estimates, one obtains a scaling law: $t_{max} \sim (\mu a/\gamma)(\gamma/\mathcal{F}V^3)^{7/6}L^{7(1-\alpha)/6\alpha}$. For a spreading following Tanner's law (1.1) with $\alpha = 1/10$ and $\mathcal{F} = \gamma$, we have $t_{max} \sim (\mu a/\gamma)L^{10.5}/V^{3.5}$. This scaling gives values of the order of 1 s for the present experiments, agreeing with the experimentally determined t_{max}. A similar result is obtained with $\alpha = 1/8$ and $\mathcal{F} = \rho g$. The dependence of t_{max} on a and L is checked from the measured values of t_{max} in the experiments reported in figure 5(*a*) as well as in another series of experiments performed with different L (figure 7*a*). The above-mentioned scaling law is consistent with the observed t_{max} behaviour (figure 7*b*,*c*).

https://doi.org/10.1017/jfm.2017.627 Published online by Cambridge University Press

6. Conclusion and perspectives

The motion of the advancing macroscopic edge of a liquid drop on a substrate with a positive spreading parameter is examined experimentally in the presence of spherical particles of different diameters (10–50 μm). A sharp acceleration is observed at the moment of drop–particle interaction. It makes the velocity of the macroscopic contact line ten times larger than in the absence of particle. This acceleration is preceded by the formation of a meniscus around the particle, which occurs as a consequence of the high wettability of the particle surface. The formation of the meniscus yields a Laplace pressure to drive a rapid advancing motion of the MCL. This mechanism is confirmed through comparisons with a theoretical model. The theory provides a power law for the MCL behaviour at the late stage of the interaction, which agrees with the experimental observation.

The MCL motion accelerated by particles could be applicable to the design of superhydrophilic surfaces by topological control. The surface of *Ruellia devosiana*'s leaves has superhydrophilicity and a water drop spreads out very rapidly over it (Koch *et al.* 2009). Scanning electron microscopy reveals that the leaf surface is covered by closely packed conical cells of a size similar to the particles employed in the present investigation (Koch & Barthlott 2009). On the other hand, it was shown recently that particles sparsely deposited on a surface could drastically alter the dynamics of the contact line (Bihi *et al.* 2016). It may hence be possible to realise superhydrophilicity and the consequent rapid spreading by less structured surfaces, e.g., surfaces with sparsely deposited particles. A liquid drop deposited on a hydrophilic surface covered by particles with a well-determined inter-particle distance would spread rapidly due to the energy release from extra surfaces offered by the particles, as in the situation investigated in the present work.

Acknowledgements

This work was partially supported by Grant-in-Aid for Challenging Exploratory Research from Japan Society for the Promotion of Science (JSPS) (grant no.: 16K14176). The authors acknowledge financial support from MAE (French Ministry of Foreign Affairs and International Development) as well as from JSPS through the PHC Sakura programme 'Wetting dynamics in the presence of particles'. I.U. acknowledges support by the Fund for Strategic Research Areas from Tokyo University of Science.

Appendix A. (θ_s, θ_p)-(X, φ) relationships

The axisymmetric surface governed by the zero local mean-curvature condition $\mathcal{C} = 0$ under the boundary conditions (4.1*a*,*b*) is given by

$$\frac{r}{a\sin\varphi\cos\phi} + \sqrt{\left(\frac{r}{a\sin\varphi\cos\phi}\right)^2 - 1} = \tan\left(\frac{\phi}{2} + \frac{\pi}{4}\right)\exp\left[-\frac{z - a\,(1-\cos\varphi)}{a\sin\varphi\cos\phi}\right], \tag{A 1}$$

where the angle ϕ formed by the surface with the vertical at the MCL-p has been introduced for brevity: $\phi = \theta_p + \varphi - \pi/2$. Applying the other boundary conditions (4.1*c*,*d*) to (A 1), one obtains the following relationships between the MCL-s coordinate X and the MCL-p coordinate φ in dimensional form:

$$\frac{X}{a} = \sin\varphi\left[\cosh\left(\frac{\tan(\varphi/2)}{\sin(\theta_p+\varphi)}\right) - \cos(\theta_p+\varphi)\sinh\left(\frac{\tan(\varphi/2)}{\sin(\theta_p+\varphi)}\right)\right], \tag{A 2a}$$

https://doi.org/10.1017/jfm.2017.627 Published online by Cambridge University Press

$$\theta_s = \operatorname{arccot}\sqrt{\left(\frac{X/a}{\sin\varphi\,\sin(\theta_p+\varphi)}\right)^2 - 1}. \tag{A 2b}$$

Solving these two equations with respect to θ_s and θ_p, one obtains the functional relationships $\theta_s = \theta_s(X, \varphi)$ and $\theta_p = \theta_p(X, \varphi)$.

Appendix B. Qualitative analysis of Laplace pressure relaxation in a meniscus

The relaxation process of the Laplace pressure p_L in the meniscus at the particle foot could be analysed qualitatively by following a scaling argument given in Biance *et al.* (2004). The pressure p_L is estimated as γ/δ, where $\delta = X^2/a$ and its reciprocal represent the height and the curvature of a meniscus, respectively. The gradient of p_L is thus written dimensionally as p_L/X. This driving force would be balanced by the viscous force f_v, as the viscosity dominates over the inertia in the present experiments. Writing $f_v \sim \mu\dot{X}/\delta^2$ and substituting it into the balance $p_L/X \sim f_V$, one obtains $\dot{X} \sim \gamma X/\mu a$. The relaxation would hence be expected to occur at a time scale $\mu a/\gamma$. The fact that this time scale is short compared with the time scale of the development of the meniscus supports the immediate relaxation of the meniscus assumed in the model.

References

Bhushan, B., Jung, Y. C. & Koch, K. 2009 Self-cleaning efficiency of artificial superhydrophobic surfaces. *Langmuir* **25**, 3240–3248.

Biance, A.-L., Clanet, C. & Quéré, D. 2004 First steps in the spreading of a liquid droplet. *Phys. Rev.* E **69**, 016301.

Bihi, I., Baudoin, M., Butler, J. E., Faille, C. & Zoueshtiagh, F. 2016 Inverse Saffman–Taylor experiments with particles lead to capillarity driven fingering instabilities. *Phys. Rev. Lett.* **117**, 034501.

Bird, J. C., Mandre, S. & Stone, H. A. 2008 Short-time dynamics of partial wetting. *Phys. Rev. Lett.* **100**, 234501.

Bonn, D., Eggers, J., Indekeu, J., Meunier, J. & Rolley, E. 2009 Wetting and spreading. *Rev. Mod. Phys.* **81**, 739–805.

Cazabat, A. M. & Cohen Stuart, M. A. 1986 Dynamics of wetting: effects of surface roughness. *J. Phys. Chem.* **90**, 5845–5849.

Cox, R. G. 1986 The dynamics of the spreading of liquids on a solid surface. Part 1. Viscous flow. *J. Fluid Mech.* **168**, 169–194.

Dash, S., Alt, M. T. & Garimella, S. V. 2012 Hybrid surface design for robust superhydrophobicity. *Langmuir* **28**, 9606–9615.

de Gennes, P. G. 1985 Wetting: statics and dynamics. *Rev. Mod. Phys.* **57** (3), 827–863.

de Gennes, P. G., Brochard-Wyart, F. & Quéré, D. 2002 *Gouttes, Bulles, Perles et Ondes*. Belin.

Hervet, H. & de Gennes, P. G. 1984 Dynamique du mouillage: films précurseurs sur solide sec. *C. R. Acad. Sci. Ser. II* **299** (9), 499–503.

Koch, K. & Barthlott, W. 2009 Superhydrophobic and superhydrophilic plant surfaces: an inspiration for biomimetic materials. *Phil. Trans. R. Soc. Lond.* A **367**, 1487–1509.

Koch, K., Blecher, I. C., König, G., Kehraus, S. & Barthlott, W. 2009 The superhydrophilic and superoleophilic leaf surface of *Ruellia devosiana* (Acanthaceae): a biological model for spreading of water and oil on surfaces. *Functional Plant Biology* **36**, 339–350.

Li, X., Ma, X. & Lan, Z. 2010 Dynamic behavior of the water droplet impact on a textured hydrophobic/superhydrophobic surface: the effect of the remaining liquid film arising on the pillars' tops on the contact time. *Langmuir* **26** (7), 4831–4838.

https://doi.org/10.1017/jfm.2017.627 Published online by Cambridge University Press

LIU, Y., MOEVIUS, L., XU, X., QIAN, T., YEOMANS, J. M. & WANG, Z. 2014 Pancake bouncing on superhydrophobic surfaces. *Nat. Phys.* **10**, 515–519.

LOPEZ, J., MILLER, C. A. & RUCKENSTEIN, E. 1976 Spreading kinetics of liquid drops on solids. *J. Colloid Interface Sci.* **56** (3), 460–468.

MARMUR, A. 1983 Equilibrium and spreading of liquids on solid surfaces. *Adv. Colloid Interface Sci.* **19**, 75–102.

PAPADOPOULOS, P., DENG, X., MAMMEN, L., DROTLEF, D.-M., BATTAGLIARIN, G., LI, C., MÜLLEN, K., LANDFESTER, K., DEL CAMPO, A. & BUTT, H.-J. 2012 Wetting on the microscale: shape of a liquid drop on a microstructured surface at different length scales. *Langmuir* **28**, 8392–8398.

POPESCU, M. N., OSHANIN, G., DIETRICH, S. & CAZABAT, A.-M. 2012 Precursor films in wetting phenomena. *J. Phys.* **24**, 243102.

SNOEIJER, J. H. & ANDREOTTI, B. 2013 Moving contact lines: scales, regimes, and dynamical transitions. *Annu. Rev. Fluid Mech.* **45**, 269–292.

SNOEIJER, J. H. & EGGERS, J. 2010 Asymptotic analysis of the dewetting rim. *Phys. Rev.* E **82** (5), 056314.

TANNER, L. H. 1979 The spreading of silicone oil drops on horizontal surfaces. *J. Phys. D: Appl. Phys.* **12**, 1473–1484.

VOINOV, O. V. 1976 Hydrodynamics of wetting. *Fluid Dyn.* **11** (5), 714–721.

WAGNER, T., NEINHUIS, C. & BARTHLOTT, W. 1996 Wettability and contaminability of insect wings as a function of their surface sculptures. *Acta Zool. (Stockholm)* **77** (3), 213–225.

WANG, J., DO-QUAND, M., CANNON, J. J., YUE, F., SUZUKI, Y., AMBERG, G. & SHIOMI, J. 2015 Surface structure determines dynamic wetting. *Sci. Rep.* **5**, 8474.

YUAN, Q. & ZHAO, Y.-P. 2013 Multiscale dynamic wetting of a droplet on a lyophilic pillar-arrayed surface. *J. Fluid Mech.* **716**, 171–188.

https://doi.org/10.1017/jfm.2017.627 Published online by Cambridge University Press